Remarkable suppression of lattice thermal conductivity by electron-phonon scattering in iridium dioxide nanowires

Yi Tao,[1,2] Zhiliang Pan,[1] Thomas Ruch,[3] Xun Zhan,[4] Yunfei Chen,[2] Shixiong Zhang,[3,*] and Deyu Li[1,*]

[1]*Department of Mechanical Engineering, Vanderbilt University, Nashville, TN, 37235, USA*
[2]*School of Mechanical Engineering and Jiangsu Key Laboratory for Design and Manufacture of Micro-Nano Biomedical Instruments, Southeast University, Nanjing 210096, China*
[3]*Department of Physics, Indiana University, Bloomington, IN, 47405, USA*
[4]*Electron Microscope Center, Indiana University, Bloomington, IN 47405, USA*

*: Authors to whom correspondence should be addressed
E-mail: sxzhang@indiana.edu; deyu.li@vanderbilt.edu

ABSTRACT:

The well-known electrocatalyst iridium dioxide (IrO_2) has recently shown attractive topological and spin transport properties that promise applications as electrodes and spin injector/detector in oxide-based electronic and spintronic devices. So far, no study has been reported on its thermal properties that could disclose important aspects of electron and phonon interactions. Through combined experimental and modeling efforts, here we show rather high thermal conductivity of IrO_2 that is mainly attributed to phonon transport. Analysis indicates that the large lattice contribution results from the strong interatomic bonding and large difference in the atomic mass between iridium and oxygen. Interestingly, it is found that electron-phonon scattering plays a significant role and leads to a remarkable reduction in the lattice thermal conductivity.

Keywords: Iridium dioxide, thermal conductivity, electron-phonon scattering, nanowires

1. Introduction

Iridium oxides (or Iridates) are a representative family of 5d transition metal oxides which host a broad spectrum of intriguing electronic and magnetic states including spin-orbit coupled Mott insulator [1-3], topological semimetals [4, 5], multipolar order [6, 7], and spin liquid phases [8-11]. Among the family of iridates, the binary iridium dioxide holds great promise for potential applications in various fields [12-17]. For example, it is one of the best electrocatalysts in water splitting [15, 16, 18, 19] and a promising electrode in chemical sensing [20] and ferroelectric memory [17]. Furthermore, large spin Hall effect (SHE) was recently discovered in IrO_2 [14, 21], offering great opportunities for spin current-based electronics with low-energy consumption. The large SHE was suggested to be closely connected to the topological Dirac nodal line states in the system [12, 13, 22]. Most recently, orbital one- and two-channel Kondo effect was observed in IrO_2 and related oxide nanowires, providing a versatile platform to explore and engineer interacting topological states of matter [23].

Unlike its electrical and spin transport properties, thermal transport in IrO_2, which may involve contributions from both electrons and phonons, has been rarely studied. In view of the potential implications of electron-phonon (e-ph) interactions and the inevitable heat dissipation issue in various applications, it is important to explore thermal properties of IrO_2. In fact, recently, significant attention has been paid to the potentially high thermal conductivity of transition metal carbides and nitrides, with theoretical modeling efforts predicting lattice thermal conductivity values in the range of 20 to 1,000 W/mK [24-27] at room temperature. Some of these studies, and a couple of more on group six elements [28, 29] as well as low dimensional charge density wave materials $NbSe_3$ [30] and TaS_2 [31], also indicate an import role of e-ph scattering. However, most of these studies lack direct experimental evidence.

Here we report on measurements of the electrical, thermal, and thermoelectric properties of IrO_2 nanowires. The experimental data are further analyzed through theoretical modeling based on the Boltzmann transport equation (BTE) combined with density functional theory (DFT), which discloses a remarkable suppression in the lattice thermal conductivity as a result of e-ph scattering.

2. Results and discussion

IrO_2 has a tetragonal rutile structure with space group $P4_2/mnm$ and lattice constants $a=b=4.498$ Å and $c=3.154$ Å (Fig. 1a) [32]. Each iridium atom is surrounded by six oxygen atoms, yielding a distorted IrO_6 octahedron. The IrO_2 nanowires were synthesized *via* a thermal vapor transport process [33, 34] in a three-zone tube furnace with the zone temperatures set to 950°C (zone 1), 950°C (zone 2) and 600°C (zone 3), respectively. The precursor IrO_2 powder (Alfa Aesar, 99.99%) was in the center of zone 2, whereas multiple Si substrates were placed downstream from the precursor. The structure of the nanowires was characterized by transmission electron microscopy (TEM, JEOL 3200FS operated at 300 kV). Fig. 1b shows a high-resolution TEM image of a representative nanowire on which electrical and thermal transport properties were measured. The clear lattice fringes suggest the high crystalline quality of the nanowire, which is further confirmed by the selected area electron diffraction (SAED) pattern shown in the inset. The diffraction spots in the SAED were indexed by the tetragonal rutile structure, from which the nanowire axial direction was determined to be along the [001] crystallographic orientation.

The electrical and thermal conductivities, as well as the Seebeck coefficient of individual IrO_2 nanowires were measured using a well-established micro-bridge method [35-37], as illustrated in Fig. 1c. All measurements were performed from 10 to 340 K in a cryostat (Janis CCS-400/204) which has been used to study the thermophysical properties of various nanowires [30, 38-41]. The IrO_2 nanowires have an approximately rectangular cross-section (inset of Fig. 1c), resembling the tetragonal lattice in the (001) plane. The wire size was characterized by its hydraulic diameter (D_h) [30, 39], i.e., four times the reciprocal of the surface-area-to-volume ratio, which was measured from the cross-section cut open by a focused ion beam. The contacts between the nanowires and the electrodes were treated with electron beam induced deposition (EBID) of Pt/C to achieve good electrical and thermal contacts. Before the EBID processes, reagent alcohol was also used to wet the contacts, and evaporation of alcohol results in intimate contacts between the wire and the suspended membranes [42, 43]. These measures render the contact thermal resistance negligible as confirmed by the consistent measurement results from two IrO_2 nanowires of nearly identical diameter but different

suspended lengths (Fig. 1d). We believe that the relatively large contact area between a flat surface of the rectangular nanowire and the suspended membranes helps to minimize the contact thermal resistance.

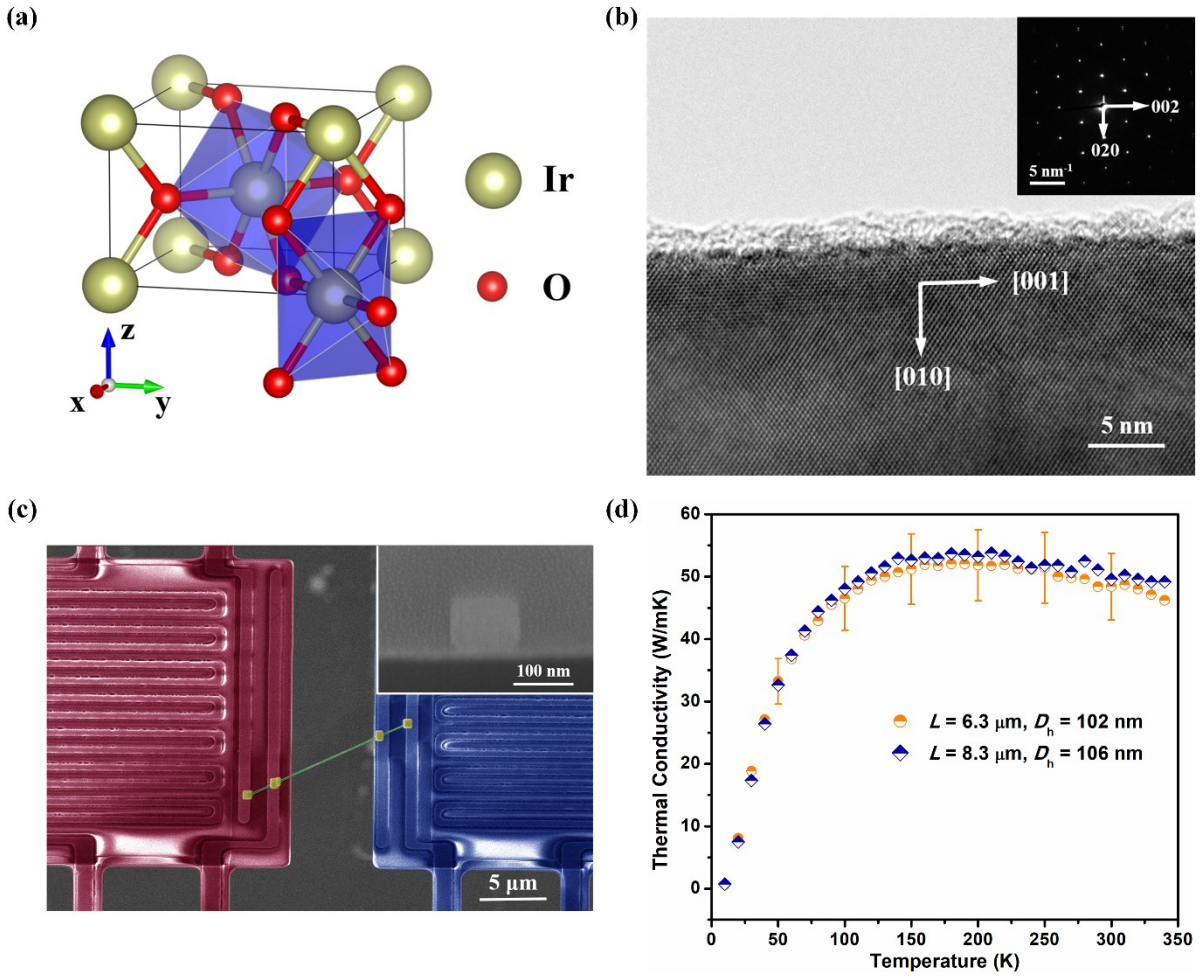

Fig. 1 (a) Crystal structure of IrO_2. (b) a high-resolution TEM micrograph of a IrO_2 nanowire. The inset shows the SAED pattern. (c) An SEM micrograph of a IrO_2 nanowire placed on the measurement device. The inset shows the cross-section of the nanowire tilted 52° from the electron beam. (d) The measured thermal conductivity of IrO_2 nanowires with different suspended lengths. The error bars are obtained by the same method reported in our previous work [38, 39].

Fig. 2a and 2b display the measured total thermal conductivity (κ_{total}), along with the lattice (κ_{ph}) and electronic (κ_e) contributions, of two IrO_2 nanowires of different hydraulic diameters (126 nm and 75 nm), respectively. κ_e was calculated based on the Wiedemann-Franz law, $\kappa_e = LT/\rho_e$, where T is the temperature, ρ_e is the measured electrical resistivity in Fig. 2c, and L is the Lorenz function estimated as follows [44]:

$$L = \frac{L_0}{1+\frac{3}{\pi^2}\left(\frac{k_F}{q_D}\right)^2\left(\frac{\theta_D}{T}\right)^2-\frac{1}{2\pi^2}\frac{J_7(\theta_D/T)}{J_5(\theta_D/T)}}\ , \tag{1}$$

where $L_0 = 2.44 \times 10^{-8}\ \mathrm{W\Omega/K^2}$ is the Sommerfeld value, $k_F = 1.23\ \mathrm{\AA^{-1}}$ is the Fermi wavevector for electrons, $q_D = 1.75\ \mathrm{\AA^{-1}}$ is the Debye wavevector for phonons, $\theta_D = 465.5\ K$ is the Debye temperature of IrO_2 and $J_n(\theta_D/T) = \int_0^{\theta_D/T} \frac{x^n e^x}{(e^x-1)^2} dx$. k_F, q_D and θ_D were obtained based on DFT calculations as detailed later. κ_{ph} was derived by subtracting κ_e from κ_{total}.

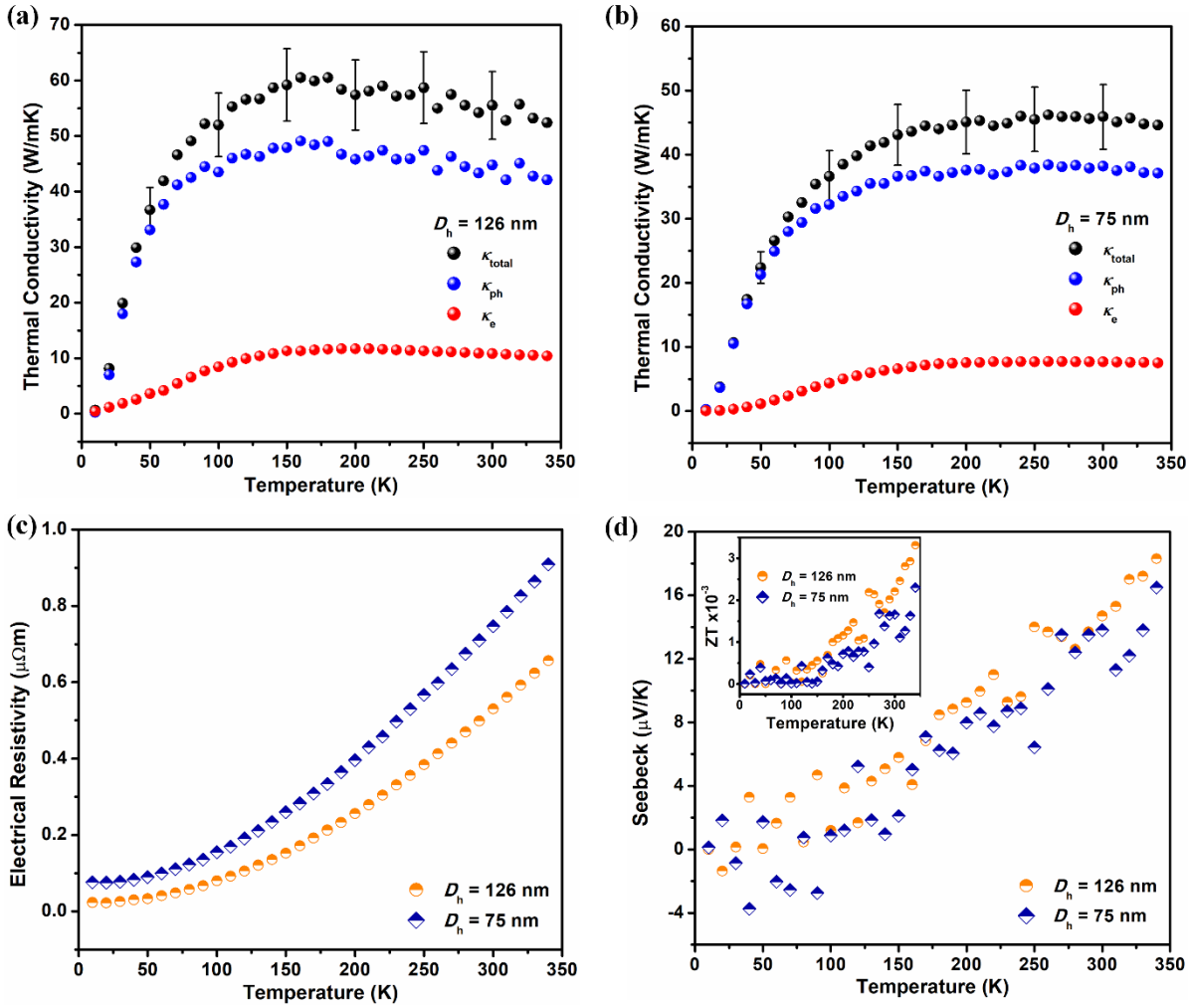

Fig. 2 The measured thermal conductivity of IrO_2 nanowires with hydraulic diameters of (a) 126 nm and (b) 75 nm. (c) The measured electrical resistivity and (d) Seebeck coefficient of the two nanowires. The inset of (d) shows the *ZT* values of the nanowires.

It is demonstrated that electrons make a non-negligible contribution to κ_{total}, because of the low electrical resistivity (or high electrical conductivity) as observed in Fig 2c. At 300 K, the ρ_e of the two nanowires are 0.53 μΩm (for $D_h = 126$ nm) and 0.75 μΩm (for $D_h =$

75 nm), both of which are in line with the reported values ranging from 0.5 μΩm to 1.2 μΩm in bulk single crystals [45]. The electrical resistivity decreases upon cooling, signifying a metallic behavior as expected in a topological semimetal [12, 13, 22]. The residual resistivity ratios ($RRR = \rho_{e,300K}/\rho_{e,10K}$, where $\rho_{e,10K}$ is the residual resistivity at 10 K) are 22.9 and 9.76 for the 126 nm and 75 nm diameter wires, respectively. Both numbers are significantly higher than the reported values in IrO_2 thin films (3.23) [21] and nanorods (1.1) [46], further confirming the high crystalline quality of our nanowires. It is worth noting, however, that bulk single crystals exhibit a *RRR* of up to 1000, depending on the crystalline quality [47]. The lower values in our nanowires may be attributed to the non-negligible boundary scattering at nanowire surface [40], as well as possible defects often formed in nanowire growth. The surface scattering argument is consistent with the fact that the thinner wire has a smaller *RRR* but higher electric resistivity. While the resistivities of the IrO_2 nanowires at 300 K are over one order of magnitude higher than that of copper and silver nanowires (~0.02 μΩm) with similar hydraulic diameters [40], they are still lower than most metal oxides with rutile-type structures such as WO_2, ReO_2 and MoO_2 [48]. This feature makes IrO_2 an excellent candidate for metal oxide electrodes [15-17]. The measured Seebeck coefficient is rather low (e.g. ~ 15 μV/K at 300 K, as shown in Fig. 2d), qualitatively consistent with the metallic nature of the nanowires. The low Seebeck coefficient and high thermal conductivity of IrO_2 nanowires lead to low thermoelectric figures of merit $ZT = S^2T/\kappa_{total}\rho_e$ (inset of Fig. 2 d), a common challenge in oxide thermoelectrics [49].

We now turn to a detailed discussion of thermal transport in the nanowires, which is the focus of this work. First, unlike most metals in which phonons only play a minor role in thermal transport [39], κ_{ph} for the IrO_2 nanowires contributes over 80% of κ_{total}. To explain the observed high κ_{ph}, we conducted theoretical modeling by combining Boltzmann transport equation with DFT calculations. In the modeling, the Vienna *ab initio* simulation package (VASP) was used for the DFT calculation [50]. An energy cut-off of 520 eV was chosen for the plane wave basis sets in the projector augmented wave (PAW) method [51]. The exchange correlation interaction was treated with the general gradient approximation (GGA) in the Perdew-Burke-Ernzerhof (PBE) parametrization [52]. A 3×3×3 supercell was employed for second-order and third-order calculations. Only interactions up to the nineth nearest neighbors

were considered in the third-order calculations. The dielectric tensor and Born effective charges were also obtained to account for long-range electrostatic interactions. A converged bulk value of the lattice thermal conductivity was obtained by solving the phonon BTE under the relaxation time approximation with a 13×13×13 q-point grid as implemented in the ShengBTE code as follows [53]:

$$\kappa_{ph,\alpha} = \frac{1}{k_B T^2 \Omega N} \sum_\lambda f_0(f_0+1)(\hbar\omega_\lambda v_\lambda^\alpha)^2 \tau_\lambda \ , \quad (2)$$

where the sub- and superscript α denotes the direction of thermal conductivity, which is along the z-axis (i.e. [001] axis) in this calculation, k_B is the Boltzmann constant, N is the number of q points, Ω is the volume of the unit cell, λ is the phonon mode with branch p and wave vector q. f_0 is the equilibrium Bose-Einstein distribution, $\hbar$ is the reduced Planck constant, ω is the phonon frequency, and v is the group velocity. τ_λ is the total relaxation time of phonon mode λ.

The blue dash line in the inset of Fig. 3a shows the calculated lattice thermal conductivity of bulk IrO_2 considering only three-phonon scattering. The value along the z-axis reaches 166 W/mK at 300 K. Note that the mass of the iridium atom in IrO_2 is nearly twelve times that of oxygen atom, a ratio that is even larger than the corresponding value of boron arsenide (BAs), which has been recently shown to possess very high thermal conductivity [54-57]. It was long believed that a crystal with high thermal conductivity typically has a low average atomic mass, strong interatomic bonding, low anharmonicity, and simple crystal structure with less atoms per primitive crystallographic unit cell [58]. Interestingly, IrO_2 has a large average atomic mass due to the heavy iridium atoms and a complex crystal structure with six atoms per unit cell. The relatively large unit cell corresponds to a complex phonon dispersion with fifteen optical phonon branches which facilitate three-phonon scattering. Therefore, one would expect a low lattice thermal conductivity. However, the calculated lattice thermal conductivity of bulk IrO_2 considering only three-phonon scattering is even higher than that of single crystalline silicon [58, 59]. The calculated value is also higher than what was predicted (i.e. 57 W/mK without considering e-ph scattering) in MgO that has a smaller average atomic mass and simpler crystal structure [60, 61].

It has been suggested that the large energy gap between the acoustic and optical phonon

modes in BAs suppresses Umklapp scattering between phonons and contribute to the high thermal conductivity of BAs. Therefore, we examine the phonon dispersion relation of IrO_2, as shown in Fig. 3b, which have a large band gap from 11 THz to 16 THz, as a result of the large atomic mass difference of IrO_2. According to $\hbar\omega = k_B T$, below room temperature, the optical phonon branches of > 6.3 THz are not well populated, and the large energy gap renders it difficult for Umklapp scattering involving phonons in the high energy optical branches to occur (see supplementary data for details).

Along the Γ-Z path that corresponds to the nanowire axis direction (i.e. [001] axis), IrO_2 has high group velocities of 7.5 km/s and 3.5 km/s for the longitudinal acoustic (LA) mode and transverse acoustic (TA) mode, respectively, which are comparable with the corresponding values of silicon [62], implying a strong interatomic bonding in IrO_2. Importantly, Fig. 3b also indicates that the optical phonon branches below 11 THz have rather large slopes, which corresponds to quite high phonon group velocities. In fact, as shown in Fig. 3c, the maximum group velocity of these optical modes is larger than the value for TA modes, suggesting that the optical phonons below 11 THz could contribute significantly to the lattice thermal conductivity of IrO_2.

To further examine the effects of three-phonon scattering, we calculated the normal and Umklapp scattering rate in bulk IrO_2, as shown in Fig. 3d. It is demonstrated that normal scattering, which conserves the phonon momentum and hence does not pose resistance to thermal transport, dominates the three-phonon scattering process with a scattering rate that is nearly one order of magnitude higher than the Umklapp scattering rate. Note that for the acoustic phonons with low frequencies, the difference between the normal and Umklapp scattering rates become more drastic. We note that the phonon dispersion also results in a suppression of Umklapp scattering rates around 6 THz, which could contribute to the high lattice thermal conductivity as well (see supplementary data for details).

To calculate the nanowire lattice thermal conductivity, a boundary scattering rate calculated as $\tau_{b,\lambda}^{-1} = v_\lambda / D_h$, is combined with the phonon relaxation time in Eq. 2 following the Matthiessen's rule. Interestingly, even after the boundary scattering is included, the calculated lattice thermal conductivity of IrO_2 nanowires is still far higher than the measured

values, as shown in Fig. 3a. Importantly, both the experimental data and simulation results show that the nanowire thermal conductivity decreases as the wire diameter reduces, indicating that the intrinsic phonon mean free path (MFP) in bulk IrO_2 is comparable to the wire diameter.

One scattering mechanism that has not be considered in the above discussion is the e-ph scattering. As shown in a recent study of $NbSe_3$ nanowires, e-ph scattering demonstrates its signature in the lattice thermal conductivity as the charge density wave develops [30, 38]. Based on the rather high electrical conductivity of IrO_2, we consider the effects of e-ph scattering, which has been neglected in the consideration of lattice thermal conductivity for oxides [63-65].

In the elevated temperature regime, the e-ph scattering rate can be considered according to Ziman's model as [66, 67]:

$$\tau_{e-ph,\lambda}^{-1} = \frac{C^2 m_e^2 \omega_\lambda}{2\pi\rho\hbar^3 v_\lambda} , \quad (3)$$

where C is the e-ph coupling constant charactered by the deformation potential, m_e is the effective electron mass as 0.67 times free electron mass for IrO_2 [68], ρ is the mass density. Taking the e-ph scattering rate into account with the fitting parameter of C taken as 6.5 eV, whose value is in line with the theoretical values of other metal oxides [69-71], it can be seen in Fig. 3a that the calculated lattice thermal conductivity of IrO_2 nanowires with both hydraulic diameters of 126 nm and 75 nm fits well with the experimental data at temperatures above 100 K. For temperatures below 100 K, the calculated lattice thermal conductivity deviates from the experimental data as temperature decreases. This is because Eq. 3, which is independent of temperature, overestimates the e-ph scattering rate at low temperatures. In reality, it is known that e-ph scattering rate reduces as temperature drops so the discrepancy can be solved with a more accurate temperature-dependent e-ph scattering rate [44]. In fact, the calculated lattice thermal conductivity without e-ph scattering fits the experimental data well for temperatures below 50 K, because in this temperature range boundary scattering dominates the thermal transport while the three-phonon scattering and e-ph scattering become negligible.

At elevated temperatures, the calculated e-ph scattering rate is higher than the Umklapp scattering rate (Fig. 3d), manifesting the importance of e-ph scattering in the lattice thermal conductivity of IrO_2. The significant decrease of the lattice thermal conductivity, from 166

W/mK to 70 W/mK at 300 K for bulk materials as shown in the inset of Fig. 3a, represents a remarkable reduction not normally seen for e-ph scattering. For most metals with lower electrical resistivity, the e-ph scattering nearly makes negligible contributions to the lattice thermal conductivity. For example, for Cu, Ag and Au, the lattice thermal conductance is nearly unaffected by the e-ph scattering [72, 73]. This is true even though their e-ph scattering rates are around 0.02 ps^{-1}, comparable to the value for IrO_2. For Ni which has strong e-ph interactions as characterized by a high scattering rate of ~0.1 ps^{-1}, the lattice thermal conductivity only reduces by 30% [72]. This is because the weak interatomic interactions in metals lead to high three-phonon scattering rates around 1 ps^{-1}, which overshadow the effects of e-ph scattering [72]. On the other hand, for most semiconductors and insulators, while the Umklapp scattering rate is lower, the low conduction electron concentration renders an even smaller e-ph scattering rate as compared to the Umklapp scattering rate. Recently, it is demonstrated that four-phonon scattering can have significant effects on the phonon scattering rate and drastically reduce the lattice thermal conductivity of BAs [74, 75]. However, for IrO_2 which has a more complex lattice structure, our calculation suggests that four-phonon scattering only induces a minor reduction in its lattice thermal conductivity without e-ph scattering (see supplementary data for details). Therefore, neglecting four phonon scattering does not affect our conclusion that e-ph scattering suppresses the thermal conductivity of IrO_2 nanowires remarkably.

In IrO_2, the weak anharmonicity renders Umklapp scattering rates lower than the e-ph scattering rates as shown in Fig. 3d, which leads to the remarkable effect of e-ph scattering. In fact, according to the inset of Fig. 3d, the phonon MFP defined as the value below which the phonons contribute to one half of the accumulated thermal conductivity, reduces from 115 nm to 51.6 nm as a result of e-ph scattering. Nevertheless, in spite of the significant effect of e-ph scattering, the thermal conductivity of IrO_2 nanowires is still comparable to that of silicon nanowires with similar diameters [76], indicating excellent thermal property of IrO_2 nanowires.

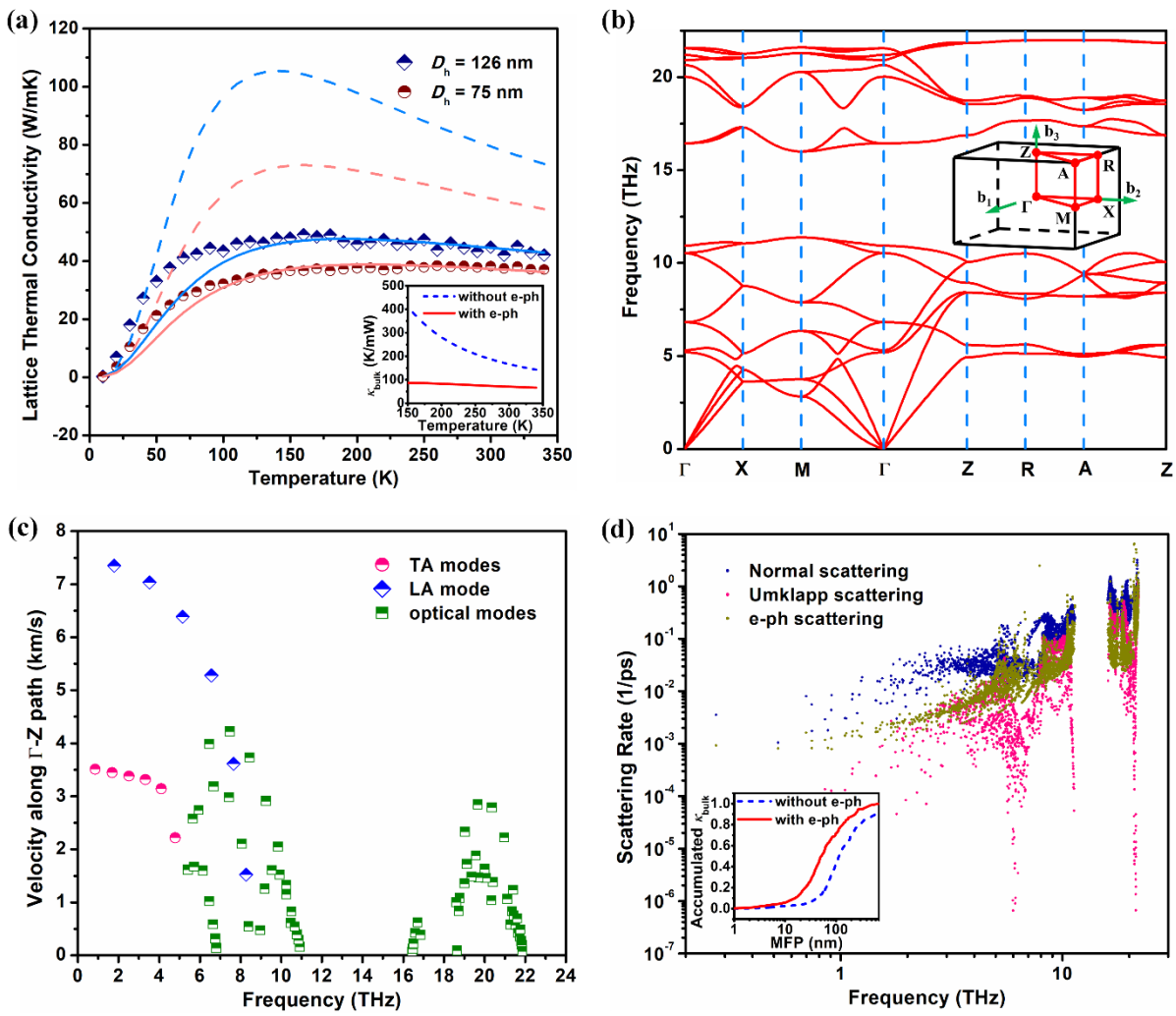

Fig. 3 (a) The measured and calculated lattice thermal conductivity of IrO_2 nanowires of 126 nm and 75 nm hydraulic diameters, where the dots show the measured results, and the dashed and solid lines show the calculated results without and with e-ph scattering, respectively. The inset shows the calculated lattice thermal conductivity of bulk IrO_2 without and with e-ph scattering along the *z*-axis. (b) The calculated phonon dispersion relation of IrO_2 along the high symmetry paths shown in the inset. (c) The phonon group velocity of IrO_2 along the Γ-Z path with different phonon modes. (d) The calculated scattering rates of IrO_2 at 300 K. The inset shows the accumulated thermal conductivity of bulk IrO_2 without and with e-ph scattering.

3. Conclusions

In summary, the electrical, thermal, and thermoelectric properties of IrO_2 nanowires were studied both experimentally and theoretically. The electrical resistivity demonstrates a metallic behavior in the entire temperature range (10-340 K) with values lower than most of the transition metal oxides. The thermal conductivity is mainly due to phonon transport, unlike in most other metals, which can be attributed to the strong interatomic bonding and large difference in the atomic mass between iridium and oxygen that correspond to high phonon

group velocities and a large energy gap from 11 THz to 16 THz. Interestingly, while electrons make less than 20% contribution to the thermal conductivity, theoretical analysis indicates that e-ph scattering suppresses the lattice thermal conductivity remarkably, which is not normally seen. The low electrical resistivity and high thermal conductivity, along with its excellent spin transport properties [14], make IrO_2 a good candidate as electrodes and spin injector/detector in oxide-based electronic and spintronic devices.

Credit author statement

Y.T. and Z.P. conducted thermal/electrical property measurements. Y.T preformed theoretical modeling. T.R. synthesized the materials. X.Z. performed TEM studies. Y.T. prepared the manuscript. S.Z. and D.L. supervised the project and edited the manuscript. All authors discussed the results and commented on the manuscript.

Declaration of competing interest

The authors declare that they have no known competing financial interests or personal relationships that could have appeared to influence the work reported in this paper.

Acknowledgements

The authors thank the financial support from the U.S. National Science foundation (DMR-1532107 and ECCS-1936406). Y.T. acknowledges financial support from the Scientific Research Foundation of Graduate School of Southeast University (Grant No. YBJJ1748) and the Postgraduate Research & Practice Innovation Program of Jiangsu Province (Grant No. KYCX17_0058).

Appendix A.

Supplementary data to this article can be found online at [doi link].

Data Availability

The raw data required to reproduce these findings are available to download from [to be provided upon acceptance]. The processed data required to reproduce these findings are available to download from [to be provided upon acceptance].

References

[1] B.J. Kim, H. Ohsumi, T. Komesu, S. Sakai, T. Morita, H. Takagi, T. Arima, Science, 323 (2009) 1329-1332.

[2] Y.K. Kim, O. Krupin, J.D. Denlinger, A. Bostwick, E. Rotenberg, Q. Zhao, J.F. Mitchell, J.W. Allen, B.J. Kim, Science, 345 (2014) 187-190.

[3] B.J. Kim, H. Jin, S.J. Moon, J.Y. Kim, B.G. Park, C.S. Leem, J. Yu, T.W. Noh, C. Kim, S.J. Oh, J.H. Park, V. Durairaj, G. Cao, E. Rotenberg, Physical Review Letters, 101 (2008) 076402.

[4] X. Wan, A.M. Turner, A. Vishwanath, S.Y. Savrasov, Physical Review B, 83 (2011) 205101.

[5] T. Kondo, M. Nakayama, R. Chen, J.J. Ishikawa, E.G. Moon, T. Yamamoto, Y. Ota, W. Malaeb, H. Kanai, Y. Nakashima, Y. Ishida, R. Yoshida, H. Yamamoto, M. Matsunami, S. Kimura, N. Inami, K. Ono, H. Kumigashira, S. Nakatsuji, L. Balents, S. Shin, Nature Communications, 6 (2015) 10042.

[6] T. Liang, Timothy H. Hsieh, Jun J. Ishikawa, S. Nakatsuji, L. Fu, N.P. Ong, Nature Physics, 13 (2017) 599-603.

[7] E.Y. Ma, Y.-T. Cui, K. Ueda, S. Tang, K. Chen, N. Tamura, P.M. Wu, J. Fujioka, Y. Tokura, Z.-X. Shen, Science, 350 (2015) 538-541.

[8] J. Chaloupka, G. Jackeli, G. Khaliullin, Physical Review Letters, 105 (2010) 027204.

[9] T. Takayama, A. Kato, R. Dinnebier, J. Nuss, H. Kono, L.S.I. Veiga, G. Fabbris, D. Haskel, H. Takagi, Physical Review Letters, 114 (2015) 077202.

[10] Y. Singh, S. Manni, J. Reuther, T. Berlijn, R. Thomale, W. Ku, S. Trebst, P. Gegenwart, Physical Review Letters, 108 (2012) 127203.

[11] T. Dey, A.V. Mahajan, P. Khuntia, M. Baenitz, B. Koteswararao, F.C. Chou, Physical Review B, 86 (2012) 140405.

[12] Y. Sun, Y. Zhang, C.-X. Liu, C. Felser, B. Yan, Physical Review B, 95 (2017) 235104.

[13] X. Xu, J. Jiang, W.J. Shi, V. Süß, C. Shekhar, S.C. Sun, Y.J. Chen, S.K. Mo, C. Felser, B.H. Yan, H.F. Yang, Z.K. Liu, Y. Sun, L.X. Yang, Y.L. Chen, Physical Review B, 99 (2019) 195106.

[14] K. Fujiwara, Y. Fukuma, J. Matsuno, H. Idzuchi, Y. Niimi, Y. Otani, H. Takagi, Nature Communications, 4 (2013) 2893.

[15] S.D. Tilley, M. Cornuz, K. Sivula, M. Grätzel, Angewandte Chemie International Edition, 49 (2010) 6405-6408.

[16] C.C.L. McCrory, S. Jung, J.C. Peters, T.F. Jaramillo, Journal of the American Chemical Society, 135 (2013) 16977-16987.

[17] Y.J. Song, H.H. Kim, S.Y. Lee, D.J. Jung, B.J. Koo, J.K. Lee, Y.S. Park, H.J. Cho, S.O. Park, K. Kim, Applied Physics Letters, 76 (2000) 451-453.

[18] W. Sun, Z. Zhou, W.Q. Zaman, L.-m. Cao, J. Yang, ACS Applied Materials & Interfaces, 9 (2017) 41855-41862.

[19] S. Moon, Y.-B. Cho, A. Yu, M.H. Kim, C. Lee, Y. Lee, ACS Applied Materials & Interfaces, 11 (2019) 1979-1987.

[20] S.A.M. Marzouk, Anal Chem, 75 (2003) 1258-1266.
[21] A. Bose, J.N. Nelson, X.S. Zhang, P. Jadaun, R. Jain, D.G. Schlom, D.C. Ralph, D.A. Muller, K.M. Shen, R.A. Buhrman, ACS Applied Materials & Interfaces, 12 (2020) 55411-55416.
[22] J.N. Nelson, J.P. Ruf, Y. Lee, C. Zeledon, J.K. Kawasaki, S. Moser, C. Jozwiak, E. Rotenberg, A. Bostwick, D.G. Schlom, K.M. Shen, L. Moreschini, Physical Review Materials, 3 (2019) 064205.
[23] S.-S. Yeh, T.-K. Su, A.-S. Lien, F. Zamani, J. Kroha, C.-C. Liao, S. Kirchner, J.-J. Lin, Nature Communications, 11 (2020) 4749.
[24] S. Li, A. Wang, Y. Hu, X. Gu, Z. Tong, H. Bao, Materials Today Physics, 15 (2020) 100256.
[25] A. Kundu, J. Ma, J. Carrete, G.K.H. Madsen, W. Li, Materials Today Physics, 13 (2020) 100214.
[26] C. Li, N.K. Ravichandran, L. Lindsay, D. Broido, Physical Review Letters, 121 (2018) 175901.
[27] A. Kundu, X. Yang, J. Ma, T. Feng, J. Carrete, X. Ruan, G.K.H. Madsen, W. Li, Physical Review Letters, 126 (2021) 115901.
[28] S. Wen, J. Ma, A. Kundu, W. Li, Physical Review B, 102 (2020) 064303.
[29] Y. Chen, J. Ma, W. Li, Physical Review B, 99 (2019) 020305.
[30] L. Yang, Y. Tao, J. Liu, C. Liu, Q. Zhang, M. Akter, Y. Zhao, T.T. Xu, Y. Xu, Z. Mao, Y. Chen, D. Li, Nano Letters, 19 (2019) 415-421.
[31] H. Liu, C. Yang, B. Wei, L. Jin, A. Alatas, A. Said, S. Tongay, F. Yang, A. Javey, J. Hong, J. Wu, Advanced Science, 7 (2020) 1902071.
[32] S.R. Butler, J.L. Gillson, Materials Research Bulletin, 6 (1971) 81-89.
[33] Y. Lee, M. Kang, J.H. Shim, N.-S. Lee, J.M. Baik, Y. Lee, C. Lee, M.H. Kim, The Journal of Physical Chemistry C, 116 (2012) 18550-18556.
[34] B.S. Guiton, Q. Gu, A.L. Prieto, M.S. Gudiksen, H. Park, Journal of the American Chemical Society, 127 (2005) 498-499.
[35] P. Kim, L. Shi, A. Majumdar, P.L. McEuen, Physical Review Letters, 87 (2001) 215502.
[36] L. Shi, D. Li, C. Yu, W. Jang, D. Kim, Z. Yao, P. Kim, A. Majumdar, J. Heat Transfer, 125 (2003) 881-888.
[37] M.C. Wingert, Z.C.Y. Chen, S. Kwon, J. Xiang, R. Chen, Review of Scientific Instruments, 83 (2012) 024901.
[38] Z. Pan, L. Yang, Y. Tao, Y. Zhu, Y.-Q. Xu, Z. Mao, D. Li, Physical Chemistry Chemical Physics, 22 (2020) 21131-21138.
[39] Y. Zhao, M.L. Fitzgerald, Y. Tao, Z. Pan, G. Sauti, D. Xu, Y.-Q. Xu, D. Li, Nano Letters, 20 (2020) 7389-7396.
[40] Y. Tao, Y. Zhao, M. Akter, T.T. Xu, Y. Chen, D. Li, Applied Physics Letters, 118 (2021) 153105.
[41] L. Yang, Y. Tao, Y. Zhu, M. Akter, K. Wang, Z. Pan, Y. Zhao, Q. Zhang, Y.-Q. Xu, R. Chen, T.T. Xu, Y. Chen, Z. Mao, D. Li, Nat Nanotechnol, (2021).
[42] J. Yang, Y. Yang, S.W. Waltermire, X. Wu, H. Zhang, T. Gutu, Y. Jiang, Y. Chen, A.A. Zinn, R. Prasher, T.T. Xu, D. Li, Nat Nanotechnol, 7 (2011) 91.
[43] L. Yang, Q. Zhang, Z. Cui, M. Gerboth, Y. Zhao, T.T. Xu, D.G. Walker, D. Li, Nano Letters, 17 (2017) 7218-7225.
[44] T.M. Tritt, Thermal conductivity: theory, properties, and applications, Springer Science & Business Media, 2005.
[45] J.J. Lin, S.M. Huang, Y.H. Lin, T.C. Lee, H. Liu, X.X. Zhang, R.S. Chen, Y.S. Huang, Journal of Physics: Condensed Matter, 16 (2004) 8035-8041.
[46] Y.H. Lin, Y.C. Sun, W.B. Jian, H.M. Chang, Y.S. Huang, J.J. Lin, Nanotechnology, 19 (2008) 045711.
[47] W.D. Ryden, A.W. Lawson, C.C. Sartain, Physical Review B, 1 (1970) 1494-1500.
[48] D.B. Rogers, R.D. Shannon, A.W. Sleight, J.L. Gillson, Inorganic chemistry, 8 (1969) 841-849.
[49] J. He, Y. Liu, R. Funahashi, Journal of Materials Research, 26 (2011) 1762.

[50] G. Kresse, J. Furthmüller, Computational Materials Science, 6 (1996) 15-50.
[51] G. Kresse, D. Joubert, Physical Review B, 59 (1999) 1758-1775.
[52] J.P. Perdew, K. Burke, M. Ernzerhof, Physical Review Letters, 77 (1996) 3865-3868.
[53] W. Li, J. Carrete, N. A. Katcho, N. Mingo, Computer Physics Communications, 185 (2014) 1747-1758.
[54] L. Lindsay, D.A. Broido, T.L. Reinecke, Physical Review Letters, 111 (2013) 025901.
[55] J.S. Kang, M. Li, H. Wu, H. Nguyen, Y. Hu, Science, (2018).
[56] S. Li, Q. Zheng, Y. Lv, X. Liu, X. Wang, P.Y. Huang, D.G. Cahill, B. Lv, Science, 361 (2018) 579-581.
[57] F. Tian, B. Song, X. Chen, N.K. Ravichandran, Y. Lv, K. Chen, S. Sullivan, J. Kim, Y. Zhou, T.-H. Liu, M. Goni, Z. Ding, J. Sun, G.A.G. Udalamatta Gamage, H. Sun, H. Ziyaee, S. Huyan, L. Deng, J. Zhou, A.J. Schmidt, S. Chen, C.-W. Chu, P.Y. Huang, D. Broido, L. Shi, G. Chen, Z. Ren, Science, 361 (2018) 582-585.
[58] G.A. Slack, Journal of Physics and Chemistry of Solids, 34 (1973) 321-335.
[59] K. Esfarjani, G. Chen, H.T. Stokes, Physical Review B, 84 (2011) 085204.
[60] N. de Koker, Physical Review Letters, 103 (2009) 125902.
[61] E. Langenberg, E. Ferreiro-Vila, V. Leborán, A.O. Fumega, V. Pardo, F. Rivadulla, Apl Mater, 4 (2016) 104815.
[62] C. Marchbanks, Z. Wu, Journal of Applied Physics, 117 (2015) 084305.
[63] J. He, S. Hao, Y. Xia, S.S. Naghavi, V. Ozoliņš, C. Wolverton, Chemistry of Materials, 29 (2017) 2529-2534.
[64] J.S. Tse, N.J. English, K. Yin, T. Iitaka, The Journal of Physical Chemistry C, 122 (2018) 10682-10690.
[65] S. Chae, K.A. Mengle, R. Lu, A. Olvera, N. Sanders, J. Lee, P.F.P. Poudeu, J.T. Heron, E. Kioupakis, Applied Physics Letters, 117 (2020) 102106.
[66] J.M. Ziman, The Philosophical Magazine: A Journal of Theoretical Experimental and Applied Physics, 1 (1956) 191-198.
[67] D.T. Morelli, J.P. Heremans, C.P. Beetz, W.S. Yoo, H. Matsunami, Applied Physics Letters, 63 (1993) 3143-3145.
[68] S.H. Brewer, D. Wicaksana, J.-P. Maria, A.I. Kingon, S. Franzen, Chemical Physics, 313 (2005) 25-31.
[69] W.-B. Zhang, Q. Qu, K. Lai, ACS Applied Materials & Interfaces, 9 (2017) 1702-1709.
[70] S.J. Chen, Y.C. Liu, C.L. Shao, C.S. Xu, Y.X. Liu, L. Wang, B.B. Liu, G.T. Zou, Journal of Applied Physics, 99 (2006) 066102.
[71] A. Janotti, B. Jalan, S. Stemmer, C.G.V.d. Walle, Applied Physics Letters, 100 (2012) 262104.
[72] Y. Wang, Z. Lu, X. Ruan, Journal of Applied Physics, 119 (2016) 225109.
[73] A. Jain, A.J.H. McGaughey, Physical Review B, 93 (2016) 081206.
[74] T. Feng, L. Lindsay, X. Ruan, Physical Review B, 96 (2017) 161201.
[75] X. Yang, T. Feng, J. Li, X. Ruan, Physical Review B, 100 (2019) 245203.
[76] D. Li, Y. Wu, P. Kim, L. Shi, P. Yang, A. Majumdar, Applied Physics Letters, 83 (2003) 2934-2936.